



Composition and Manufacturing Effects on Electrical Conductivity of Li/FeS₂ Thermal Battery Cathodes

Emilee L. Reinholz,^{a,b,z} Scott A. Roberts,^{a,*} Christopher A. Applett,^a Jeremy B. Lechman,^a and P. Randall Schunk^{a,b}

^aSandia National Laboratories, Albuquerque, New Mexico 87185-0828, USA

^bUniversity of New Mexico, Albuquerque, New Mexico 87185-0828, USA

Electrical conductivity is key to the performance of thermal battery cathodes. In this work we present the effects of manufacturing and processing conditions on the electrical conductivity of Li/FeS₂ thermal battery cathodes. We use finite element simulations to compute the conductivity of three-dimensional microcomputed tomography cathode microstructures and compare results to experimental impedance spectroscopy measurements. A regression analysis reveals a predictive relationship between composition, processing conditions, and electrical conductivity; a trend which is largely erased after thermally-induced deformation. The trend applies to both experimental and simulation results, although is not as apparent in simulations. This research is a step toward a more fundamental understanding of the effects of processing and composition on thermal battery component microstructure, properties, and performance.

© The Author(s) 2016. Published by ECS. This is an open access article distributed under the terms of the Creative Commons Attribution Non-Commercial No Derivatives 4.0 License (CC BY-NC-ND, <http://creativecommons.org/licenses/by-nc-nd/4.0/>), which permits non-commercial reuse, distribution, and reproduction in any medium, provided the original work is not changed in any way and is properly cited. For permission for commercial reuse, please email: oa@electrochem.org. [DOI: 10.1149/2.1191608jes] All rights reserved.

Manuscript submitted March 18, 2016; revised manuscript received May 4, 2016. Published June 11, 2016. This was Paper 159 presented at the Phoenix, Arizona, Meeting of the Society, October 11–15, 2015.

Li/FeS₂ thermal battery performance relies on high electrical conductivity in the cathode at operating temperatures,¹ a property influenced by the cathode microstructure. This microstructure experiences deformation, or “slumping,” when the battery is thermally activated and the electrolyte melts. Stresses from uniaxial compression redistribute between electrolyte and FeS₂ particles as electrolyte undergoes a phase change, rearranging the cathode microstructure. From transport considerations, we assume the cathode microstructure is a three-dimensional (3D) bicontinuous network consisting of (1) fully connected solid, electrically conductive FeS₂ particles and (2) a phase consisting of the electrolyte, binder, lithiating agent, and pore space (EBLP). This composite material’s effective electrical conductivity depends on the ability to transport electrons through the connected FeS₂ network.

Ongoing research emphasizes critical links between manufacturing processes, microstructural details, material properties, and performance.² For decades, researchers have explored aspects of the process-microstructure-property-performance relationship for FeS₂ cathodes.^{3–8} However, the link between these aspects remains unexplored with respect to the pressed-powder thermal battery system. Currently the method used to manufacture pressed-powder FeS₂ cathode pellets applies empirically-determined parameters. Without a more fundamental and integrated understanding of the interactions between manufacturing, microstructure, properties, and performance, further progress will be limited.

In this paper, we analyze the relationship between composition, manufacturing, microstructure, and electrical conductivity for thermal battery cathodes. We apply techniques from previous studies, such as microcomputed tomography (MicroCT) for three-dimensional (3D) microstructure characterization^{9–15} of highly irregular geometries for use in numerical models.^{16–19} Our approach differs from prior research on FeS₂ thermal battery cathode materials because we perform an integrated investigation of the process-microstructure-process-performance relationship without relying on empirical data.

Experimental

Pellet manufacturing.—Li/FeS₂ cathode pellets were manufactured varying three pellet material and processing parameters:

FeS₂ particle size distribution (including [i] 32–38, [ii] 38–45, and [iii] 45–53 μm); FeS₂:EB (electrolyte and binder) weight ratio (including [i] 2.3, [ii] 2.9, and [iii] 3.9); and pellet density (including [i] 2.76, [ii] 2.91, and [iii] 3.06 g/cm³). Minitab²⁰ was used to perform a design of experiments (DOE) to select parameter combinations from predetermined manufacturable values. Application of Minitab’s D-optimality criteria for optimal design decreased the DOE from 27 combinations to nine of the most statistically important combinations.

Raw FeS₂ powder from a natural source was sent to Union Process, Inc. (Akron, OH), for particle size reduction with a batch dry grind process. After particle size reduction, particles were separated by size when sieved for 35 minutes with a stack of ASTM E11 sieves (Gilson Company, Inc., Lewis Center, OH) and a W.S. Tyler RO-TAP Sieve Shaker (W.S. Tyler, Mentor, OH). The sieved powder fractions were separated and baked in a vacuum oven (Binder, Tuttlingen, Germany) at 103°C for 16 hours plus several hours for the oven to cool after venting. After bakeout, all powder preparation, pellet manufacturing, and sample assembly occurred in a dry laboratory maintained at low humidity (maximum 750 ppm water, or –23°C frost point). Samples from the sieved powder fractions underwent particle size analysis with sonication in water at Union Process using a Microtrac Inc. S3000/S3500 laser diffraction particle size analyzer (Microtrac, Montgomeryville, PA). The FeS₂ particle size distributions measured with laser diffraction differed from the distributions we expected from the sieve opening sizes. Because sonication in water likely broke up observed FeS₂ particle agglomerations prior to laser diffraction measurements, our analyses of conductivity measurements apply the distributions expected from sieve openings.

The FeS₂ powders were combined in a TurbulaT2F (Willy A. Bachofen AG Maschinenfabrik, Muttenz, Switzerland) mixer with electrolyte and binder (EB) and lithiating agent powders to create three FeS₂:EB weight ratios. The EB powders included 45/55 wt % LiCl/KCl eutectic electrolyte and MgO binder (Merck), and the lithiating agent was Li₂O (Sigma-Aldrich, St. Louis, MO). Combined powders (FeS₂+EB+Li₂O) were fused and then manually broken up and sieved through a No. 60 sieve with 250 μm opening size.²¹ Fused powders were cold-pressed into 3.15 cm diameter cylindrical pellets with a Wabash 50 ton hydraulic press (Wabash MPI, Wabash, IN). Powder and pellet masses were measured with a Mettler AE 240 balance (Mettler-Toledo, LLC, Columbus, OH). However, the achieved pellet densities did not precisely meet target values due to experimental limitations. For this reason, measured densities were applied in all analyses, rather than target values.

*Electrochemical Society Member.

^zE-mail: elreinh@sandia.gov

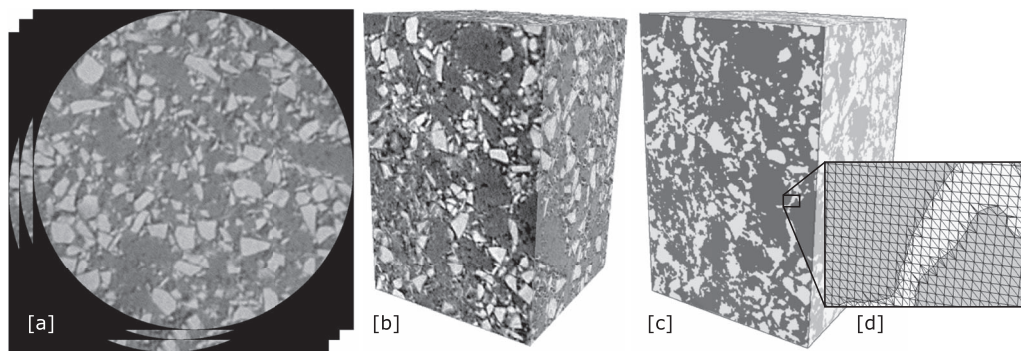


Figure 1. Reconstruction of a microstructure from MicroCT characterization. (a) TIFF images of cathode cross-sections produced by MicroCT. The light gray regions are FeS_2 ; the medium gray is electrolyte, binder, and lithiating agent; and the darkest regions are voids. (b) Volume reconstructed from TIFF files and cropped to a $300\ \mu\text{m} \times 300\ \mu\text{m} \times 500\ \mu\text{m}$ volume. (c) Binarized microstructure used for surface meshing. (d) Magnified view of the mesh after application of CDFEM.

Electrical conductivity measurements.—Impedance spectroscopy (Solartron SI 1287 Electrochemical Interface and Schlumberger SE 1255 Frequency Response Analyzer, AMETEK, Inc., Berwyn, PA) was applied to determine the electrical conductivity of each cathode using a parallel configuration through the pellet thickness, where individual pellets were sandwiched between two stainless steel electrodes and uniaxially compressed. Impedance spectroscopy settings included 10 mV peak to peak voltage input from 10 kHz to 1 Hz, controlled using commercial software.²² Cathode temperature was controlled and measured with a Honeywell temperature controller (Honeywell, Morristown, NJ), and a weight stage applied 831 kPa of uniaxial pressure. Negligible inductance and capacitance permitted use of the Z' intercept to determine sample resistance at low frequency. Electrical conductivity was calculated from each pellet's resistance with adjustments for the cathode geometry.

Cathode impedance measurements of solid-state pellets were taken before and after slumping. Slumping was induced by heating each cathode to 500°C for two minutes under compression in the parallel configuration, immediately followed by cooling and resolidification. The impedance was measured when cathodes were brought to thermal equilibrium at either 25, 100, or 200°C .

Microstructure Representation

Because we sought to model as much of the 3D microstructure of highly irregular FeS_2 particles as possible, we chose to develop experimental microstructure representations using MicroCT for characterization. We characterized pre- and post-slumped samples of each pellet type with a ZEISS Xradia 520 Versa 3D X-ray microscope (Carl Zeiss Microscopy GmbH, Jena, Germany) and achieved approximately $0.1\ \text{mm}^3$ volumes with $0.5\ \mu\text{m}$ pixel size as shown in Figure 1a.

Figure 1 illustrates the workflow to generate microstructure representations from 3D MicroCT images using Avizo software.²³ First, 2D slices were reconstructed into a 3D volume by importing the slices as a stack of TIFF files into Avizo (Figures 1a and 1b). The microstructures were binarized using Avizo's Watershed algorithm (Figure 1c). The two phases included an electrically conductive phase (FeS_2) phase and a far less conductive phase (electrolyte, binder, lithiating agent, and pore, or EBLP). Subtraction of the EBLP phase isolated the FeS_2 particles to form representative geometries for the computational simulations. Then, geometries were smoothed, meshed with a triangular surface mesh, and exported with the STL file format for computational simulations. Last, we applied the Conformal Decomposition Finite Element Method (CDFEM)²⁴ to convert each particle mesh and nonconformal background mesh to a conformal mesh (Figure 1d). The reader is referred to Roberts et al.²⁵ for a description of CDFEM and its advantages for meshing complex geometries, and to the Mesh resolution and Domain volume sections of the Appendix for geometry and mesh verification details.

Model

Governing equation and boundary conditions.—Conductive materials behave according to Ohm's law, which forms Equation 1 when combined with the steady-state continuity equation for current,

$$\nabla \cdot (\sigma \nabla V) = 0. \quad [1]$$

In this equation, σ represents the electrical conductivity tensor and V represents the voltage.

Equation 1 is solved on the geometry described in "Microstructure Representation" and idealized in Figure 2 assuming (1) isotropic conductivity, (2) no contact resistance between particles, and (3) uniform properties throughout each phase of the material. There is significant variability and uncertainty in the experimental data for the electrical conductivities of each pure phase. Therefore, we selected nominal values that are order-of-magnitude consistent with the data that exists, with $\sigma_{\text{FeS}_2} = 10\ 1/(\Omega\text{m})$ and $\sigma_{\text{EBLP}} = 0.01\ 1/(\Omega\text{m})$. See the "Model physics" in the Appendix for a description of the selection of σ_{FeS_2} and σ_{EBLP} . Figure 2 also illustrates application of boundary conditions to the cathode microstructure. We applied a constant voltage on outer surfaces normal to the x -axis. On the outer surfaces normal to the

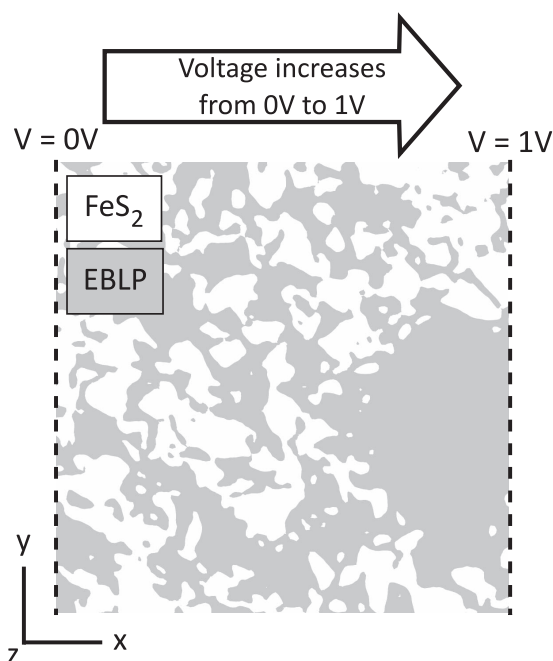


Figure 2. Boundary conditions applied to a cross-section of the cathode microstructure.

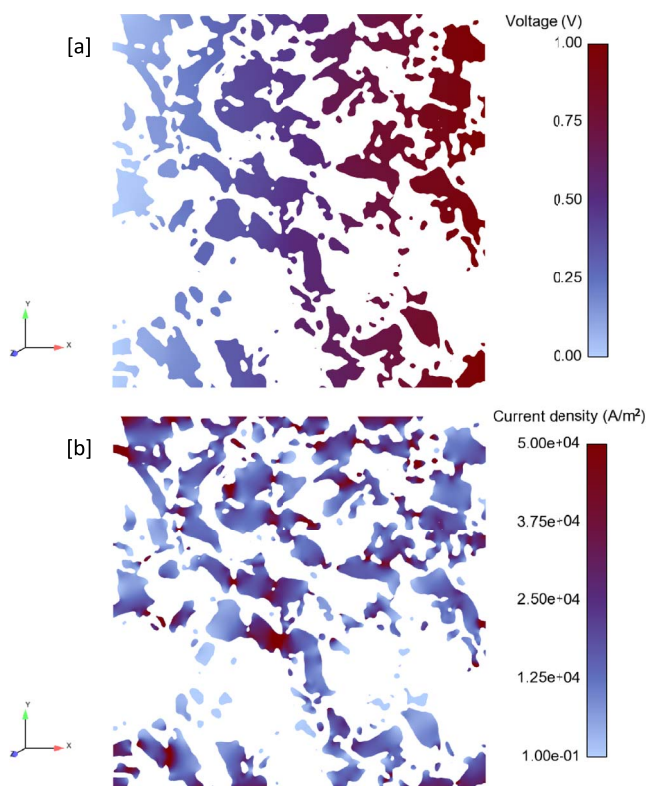


Figure 3. Results of Equation 1 applied to one cathode microstructure. A cross-section of the isolated particle phase is shown. (a) Electric potential, or voltage, field. (b) Current density vector, with magnitude indicated.

y- and z-axes, we applied a linear voltage ramp,

$$V(x) = \frac{1}{L}x, \quad [2]$$

where L is the length of the domain in the x -direction and x is the spatial location within the model domain.

Numerical methods.—Aria, a coupled multiphysics Galerkin finite element program within Sierra Mechanics,²⁶ was used to solve Equation 1 on meshes with first-order tetrahedral elements. The model domain was a cube with 300 μm edges and 130×10^6 elements with 1.25 μm edges. The element size was determined by memory limitations and is discussed further in the Mesh resolution section of the Appendix. We used Newton's method for the nonlinear solver, and an iterative method of conjugate gradients (CG) and Jacobi preconditioning to solve the system of linear equations.

Figure 3 depicts results on a cross-section of the cathode microstructure. The voltage ramp increases along the x -axis with local variations due to the microstructure. The current density flows in the opposite direction of increasing voltage. The current density appears greatest through narrow connections between conductive particles.

Regression analysis.—Regression analysis techniques were applied using Minitab to correlate the electrical conductivity with changes to the processing and composition parameters. The regression analysis included all first-order terms and second-order interactions involving four continuous input variables: as-pressed pellet density (ρ), the mean of each target particle size distribution (α), FeS₂:EB weight ratio (ϕ), and temperature (T , in Kelvin),

$$\sigma = C_1 + C_2\rho + C_3\alpha + C_4\phi + C_5T + C_6\rho\alpha + C_7\rho\phi + C_8\rho T + C_9\alpha\phi + C_{10}\alpha T + C_{11}\phi T. \quad [3]$$

A forward stepwise regression was used to determine the most significant terms from Equation 3 for each dataset, and insignificant terms were eliminated.

To quantify the sensitivity of conductivity to each input variable, the terms remaining in Equation 3 were differentiated with respect to each variable, then scaled by the mean value of that variable and the mean conductivity. This results in the sensitivity expression:

$$S(v) = \frac{\partial \sigma}{\partial v} \frac{v_{\text{mean}}}{\sigma_{\text{mean}}} \text{ where } v \subseteq \{\rho, \alpha, \phi, T\}. \quad [4]$$

For experimental calculations, the mean conductivity was from the 25°C measurements. Scaling by σ_{mean} and v_{mean} was necessary to compare experimental and simulation sensitivities, since the simulation results depend on the specified conductivities and σ_{FeS_2} can vary widely.²⁷

Results and Discussion

The results of all experiments, simulations, and regression analyses are presented in Figures 4–6. Figure 4 shows the effects of processing, composition, and temperature on the experimental electrical conductivity before and after slumping. Prior to slumping (Figures 4a–4c), conductivity increased with temperature, density, and FeS₂ composition. After slumping (Figures 4d–4f), the mean conductivities increased overall and continued to increase with temperature. However, overlapping standard deviations indicate significant variability among replicates.

The simulation results are depicted in Figure 5 and are plotted with respect to spatial densities that were approximated by the volume of FeS₂ and EBLP present in each computational domain. The effective conductivity is shown divided by σ_{FeS_2} to scale σ_{eff} by the electrical properties selected for the model (see “Model physics” in the Appendix). In the pre-slumped data (Figure 5a) from FEM simulations, no trend due to processing or composition parameters is visible, and the results appear random. However, a relationship between density and conductivity appears in the post-slumped results (Figure 5b). More data could help to determine the strength of this relationship. Temperature dependence was not included in the simulations because the electrical conductivity of natural FeS₂ can vary widely at a single temperature²⁷ and characterization of raw FeS₂ electrical properties was not included in this research.

Lastly, Figure 6 illustrates the sensitivity of the regression results to each studied parameter. From the sensitivity analysis (Equation 4), the most important pre-slump experimental parameters (Figure 6) include density and temperature, followed by particle size distribution and composition. The most important post-slump simulation parameters (Figure 6) are density and particle size distribution. Sensitivity analyses of the post-slump experimental data and the pre-slump simulation data are not provided because a statistical analysis revealed poor predictive value, as measured by residual plots and R^2 values.

The results from the pre-slump experimental data and its associated sensitivity analysis correlate well. Figures 4a–4c and 6 both show clear effects due to density, composition, and temperature. These trends make sense. Conductivity increased with density because greater density should increase contact between particles, allowing better conduction of electricity through the microstructure. Similarly, greater FeS₂ content, indicated by a higher FeS₂:EB weight ratio, provided more conductive particles available for electrical conduction. The conductivity increase with temperature was expected due to the semiconducting properties of FeS₂. As temperature increases, greater thermal energy excites an increasing population of electrons across the conduction band.²⁸ The effect of the last parameter, the FeS₂ particle size distribution, is unclear from visual inspection of Figures 4a–4c. However, the sensitivity analysis reveals its importance in Figure 6. The trend here shows that conductivity decreases with increasing mean particle size. Within a domain of constant volume, which is the case here, increasing particle size reduces contact area between conductive particles, but as the particle radius decreases, more contact area is possible. Greater interparticle contact improves the number of

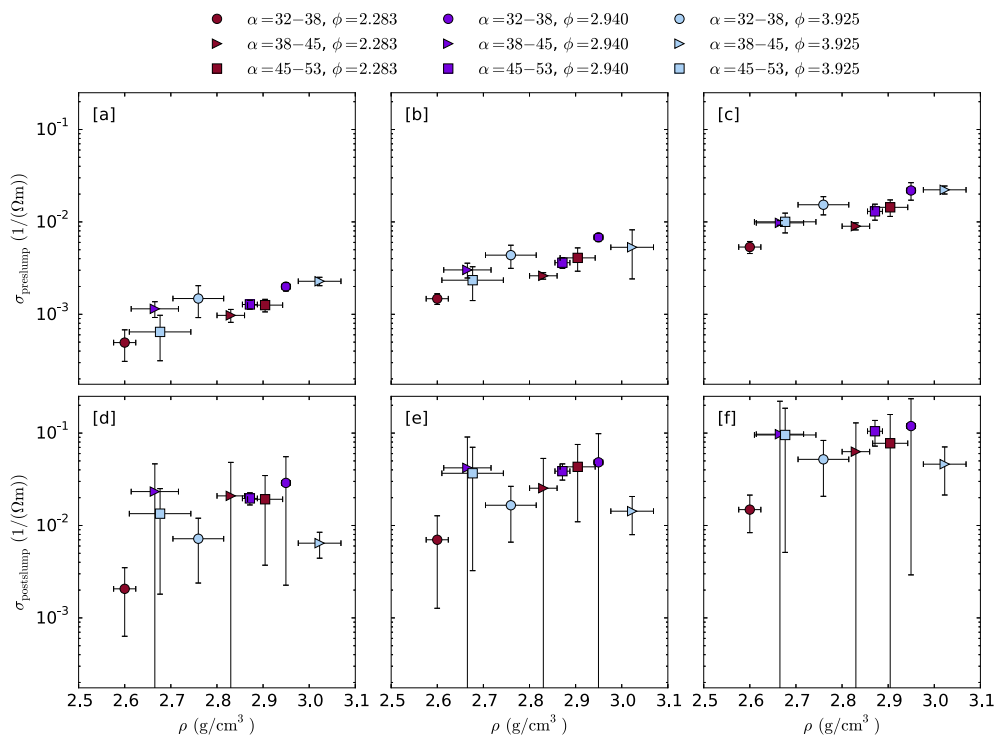


Figure 4. Mean electrical conductivity of experimental data for preslumped samples at (a) 25, (b) 100, and (c) 200°C, and postslumped samples at (d) 25, (e) 100, and (f) 200°C. Variables included particle size distribution (α), FeS₂:EB weight ratio (ϕ), and pellet density (ρ). Error bars represent standard deviations, calculated from triplicate samples.

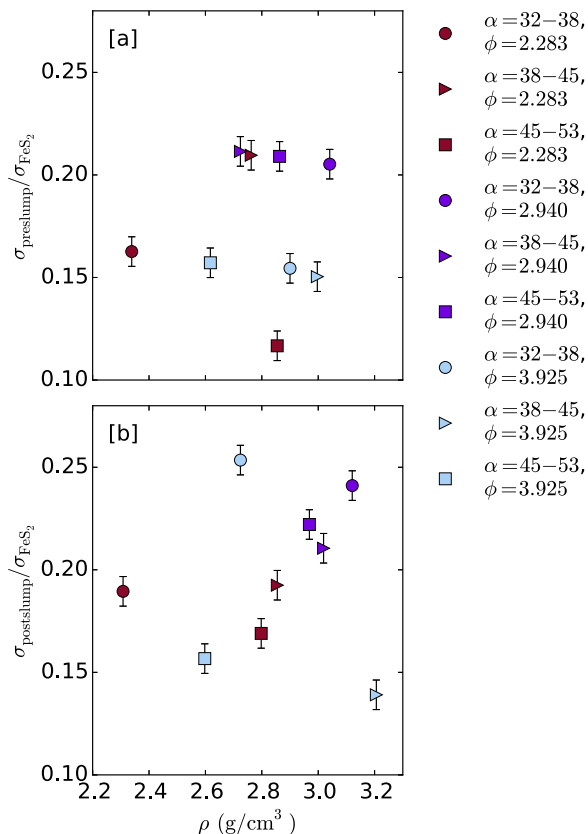


Figure 5. Effective electrical conductivity relative to FeS₂ of (a) preslumped and (b) postslumped simulations. Error bars represent standard deviations expected for this domain size,³¹ discussed under “Domain Volume” in the Appendix.

electron transport pathways and increases conductivity. The experimental preslump results reveal links between the composition and processing parameters, the microstructure, and physics relevant for the property of electrical conductivity.

In contrast, the preslump simulation results (Figure 5a) show little change in the effective electrical conductivity due to composition or processing variables. These results do not agree well with the preslump experimental results (Figures 4a–4c) and produced a statistically weak regression model for sensitivity analysis. Yet, the purpose of the mesoscale simulations was to probe effects of processing and composition on microstructures derived directly from the tested samples. Because the simulations and experiments did not predict the same behavior, we sought to understand the discrepancies between the two

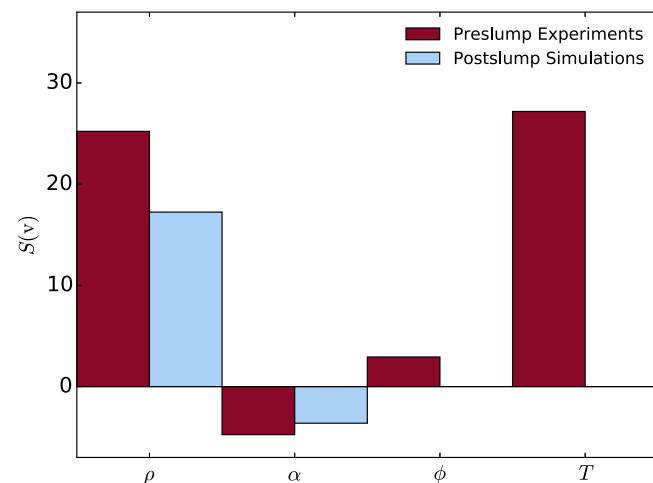


Figure 6. Plot of sensitivity results (Equation 4) from preslump experiments and postslump simulations.

datasets through verification studies, described throughout the Appendix. From these studies we found that the preslump simulation results may not have correlated well with experimental data because of limits on the accuracy and volume of the microstructure representation, computational limitations on the mesh resolution and domain volume, and exclusion of potentially important physics, such as interparticle contact resistance.

The highly variable postslump experimental results (Figures 4d–4f) show that the effect of processing and composition, within the ranges tested, appears erased after slumping. This variability led to a statistically weak regression model for sensitivity analysis. We hypothesize that such variability may be due to exposure of oxidized FeS₂ particle surfaces to molten electrolyte during slumping. During manufacturing, the FeS₂ was exposed to oxygen, and prior to bake-out, the powder was also exposed to ambient humidity. Oxidation of FeS₂ can occur within minutes of exposure to oxygen or moisture,²⁹ so it is possible that oxide layers formed on the FeS₂ particles, and the preslump conductivity results were more consistent due to contact between particles with oxide layers. During slumping, exposure of the molten electrolyte to the FeS₂ particles may have removed the oxide layers from FeS₂ particles. If this is the case, after slumping, clean FeS₂ particle surfaces were in physical contact during measurements. Because the cathode conductivity results showed significant variability among replicates, this suggests that the conductivity may have been impacted by minor and trace elements within FeS₂ which can cause the conductivity of natural FeS₂ to vary by four orders of magnitude at one temperature.²⁷ We know little about the source and chemical composition of the FeS₂ used, but better characterization, cleaning of FeS₂ particles to remove oxide layers prior to pellet formation, and maintenance in an inert atmosphere, could help evaluate the validity of this hypothesis. Whether it is true, the effect of confounding variables is apparent and was enhanced by the slumping process.

Visual inspection of Figure 5b indicates that simulations of postslump cathode pellets provided far less noisy results, but the link between the parameters tested and conductivity is unclear. A slight upward trend of conductivity with density is seen, however confirmation with more data would be helpful. The associated sensitivity analysis, plotted in Figure 6, unmask the links between density, FeS₂ particle size distribution, and electrical conductivity, where the conductivity is most sensitive to density. Density and particle size distribution were also found important in the sensitivity analysis of the experimental preslump data, though the sensitivity values differ by two orders of magnitude. Figure 5b also illustrates that the influence of FeS₂:EB weight ratio was not found to be significant in the sensitivity analysis of postslump simulations. Temperature was not significant because it was not a variable in the simulations.

The sensitivity analysis results for the postslump simulations show that the applied simulation method can be a useful tool to study the process-microstructure-property relationship for thermal battery cathodes. Using this simulation method, combined with a sensitivity analysis of a regression model, we observed effects of composition and processing on the microstructure and electrical conductivity after slumping, when experimental results were inconclusive. However, important limitations discussed throughout the Appendix prevented clear results in the preslump simulations, when the experimental results were more consistent. This suggests that the postslump representative geometries were overall more robust in the simulations than preslump geometries, possibly because of microstructural changes induced by slumping. More effort remains to obtain experimentally validated simulations for greater predictive value of the link between processing, microstructure, properties, and performance for thermal battery cathodes before and after slumping.

With respect to thermal battery performance, our results suggest that when a Li/FeS₂ thermal battery heats prior to activation, the thermal dependence of FeS₂'s electrical properties should make the cathode increasingly conductive, even before the electrolyte melts. When the electrolyte melts and slumping occurs, we expect that the cathode's electrical conductivity will increase further due to changes in the cathode that decrease resistance. This could improve battery

performance. The magnitude of this effect is unknown because the effect of slumping when the electrolyte is molten was not studied, but we did observe increased electrical conductivity at all temperatures in the postslump experimental results, even among the noise. In addition, a lack of uniform FeS₂ properties could impact performance. These observations could help improve thermal battery design and performance.

Conclusions

Using impedance spectroscopy and sensitivity analysis of a regression model, we found that the most influential composition and processing parameter on experimental preslump electrical conductivity is density, followed by the FeS₂ particle size and the weight ratio of FeS₂ to EBLP. These results suggest that the microstructure, shaped by processing and composition parameters, drives the electrical conductivity prior to slumping. Temperature also strongly influences the conductivity due to the semiconducting properties of FeS₂.

Highly variable postslump results suggest that conditions during slumping obscure or erase the influence of composition and processing parameters on the microstructure and electrical conductivity. We speculate that other factors affecting the electrical conductivity of FeS₂ dominate after slumping. As a semiconductor, the electrical conductivity of FeS₂ depends on temperature, minor and trace elements,²⁷ and oxidation.²⁹ We hypothesize that the FeS₂ particles, exposed to oxygen and ambient moisture during processing, may be coated in an oxide layer prior to slumping. During slumping, exposure to the molten salt removes the oxide layer from FeS₂ particles, increasing the impact of minor and trace elements in the FeS₂ on the cathode electrical conductivity as cleaned FeS₂ surfaces come into contact. Further work, particularly chemical analysis of the FeS₂ powder, is necessary to verify this hypothesis.

We also demonstrated that the microstructure of the electrically conductive phase (i.e., FeS₂ particles) can be extracted using MicroCT for reconstruction into a representative geometry for mesoscale simulations with CDFEM. Characterization and computational limitations likely prevented steady-state simulations of preslump cathodes from comparing well with experimental results. However, postslump simulations combined with sensitivity analysis of a regression model revealed the influence of density and particle size distribution on the effective electrical conductivity, a trend similar to preslump experimental results. A trend such as this was impossible to see among highly variable postslump experimental results. The difference between experimental and computational results suggests that both methods require improvement and provide many opportunities for future research.

The results we presented reveal important challenges in the combined experimental and computational investigation of the link between processing, composition, microstructure, and the electrical conductivity of pressed-powder Li/FeS₂ thermal battery cathodes. However, this work remains a step toward a more fundamental and integrated understanding of the process-microstructure-process-performance relationship.

Acknowledgments

The authors acknowledge Nick Hudak for assistance with powder acquisition and preparation; Linda Johnson for powder and pellet manufacturing; Barry Ritchey, Ryan Wixom, and Burke Kernen for MicroCT characterizations; and Lauren Wilson for her assistance with statistical analysis. We also thank David Noble, Dan Bolinteanu, and Hector Mendoza for helpful conversations concerning mesoscale CDFEM simulations, and conversations with Joe Romero, Jonathan Madson, and Fikile Brushett regarding microcomputed tomography.

Sandia National Laboratories is a multi-program laboratory managed and operated by Sandia Corporation, a wholly owned subsidiary of Lockheed Martin Corporation, for the U.S. Department of Energy's National Nuclear Security Administration under contract DEAC04-94AL85000.

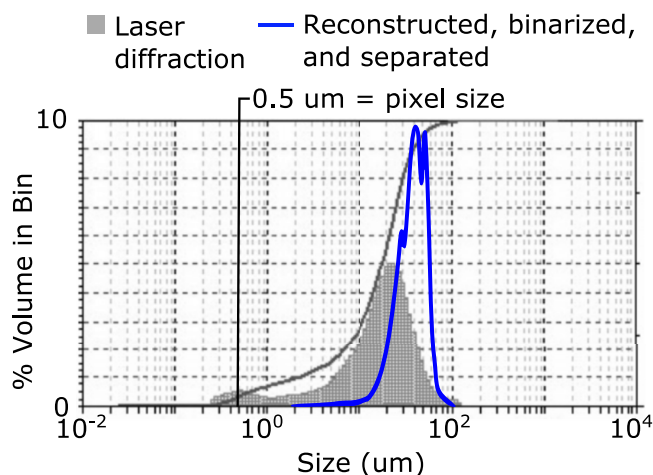


Figure A1. Comparison of laser diffraction and reconstruction FeS_2 particle size distributions for one pellet type. For the laser diffraction particle size distribution, “Size” was determined by light scattering techniques. For the distribution of the reconstructed, binarized, and separated particles, “Size” refers to the minimum Feret diameter.

Appendix

Simulation verification studies performed on cathode representative geometries indicate that the simulation results were sensitive to (1) the characterization and reconstruction method, (2) mesh resolution, (3) the simulation domain size, and (4) model physics. Studies of each of these factors and their results will be discussed throughout the following sections.

Characterization and reconstruction.—We studied microstructure reconstruction quality by comparing experimental and computational outcomes for FeS_2 particle size distributions and volume fraction. Figure A1 shows a comparison of experimentally-determined and computationally-measured particle size distributions for one pellet type. As discussed in “Pellet manufacturing,” the experimental particle size analysis included laser diffraction with sonication in water. For the computationally-measured particle size analysis, particles from the binarized reconstruction were separated and measured using Avizo. The computational results show a volume distribution similar to the experimental results, but particles smaller than $10\ \mu\text{m}$ did not appear in the reconstructed distribution. This is likely due to (1) agglomerated particles appearing as one “particle” when characterized by MicroCT yet shown separately in laser diffraction results due to sonication; (2) insufficient MicroCT resolution for the smallest particles, because $0.5\ \mu\text{m}$ pixels are insufficient to resolve features of comparable size; and (3) sensitivity of the reconstruction to image processing settings.³⁰

We also compared each microstructure reconstruction’s FeS_2 volume fraction with its experimental volume fraction, calculated from the pellet mass, volume, and chemical composition. Figure A2 illustrates the relative error of the volume fraction, calculated by comparing the volume fractions from the Watershed segmentation (binarization), surface mesh, and CDFEM mesh, to the experimental values. The binarization results were sensitive to the Watershed algorithm settings, and as the plot shows, the binarization volume fraction deviated from the experimental volume fraction by $\pm 5\%$, with a mean relative error of -1.4% . The mean relative error suggests that binarization led to volume loss for most reconstructions, which is particularly significant if this occurred where particles connect.

Binarization was followed by surface meshing. The surface mesh step included smoothing algorithms that were selected for efficient mesh generation. Since the mean error calculated from comparison of the surface mesh and binarization volume fractions was -1.8% , application of the smoothing algorithms caused volume loss in all but one reconstruction. Smoothing may have significantly filled small holes or gaps in the single reconstruction that experienced volume added. The overall relative error due to smoothing, calculated with respect to the experimental volume fraction, was within $\pm 10\%$ with a mean of 3.1% .

Finally, application of CDFEM further altered the volume fraction because the background mesh resolution was insufficient to preserve fine features in the surface mesh, such as small particles or small gaps between particles, and further mesh refinement was not possible due to memory limitations. At the finest mesh resolution, the problem was solved on a microstructure representative geometry with over 23×10^6 nodes and 130×10^6 elements. At this resolution, every reconstruction’s volume fraction changed again, and increased for most of the reconstructions. The mean relative error (calculated with respect to the surface mesh volume fraction) was 2.6% , but the relative error with respect to the experimental value remained within $\pm 10\%$ with a mean of -0.6% .

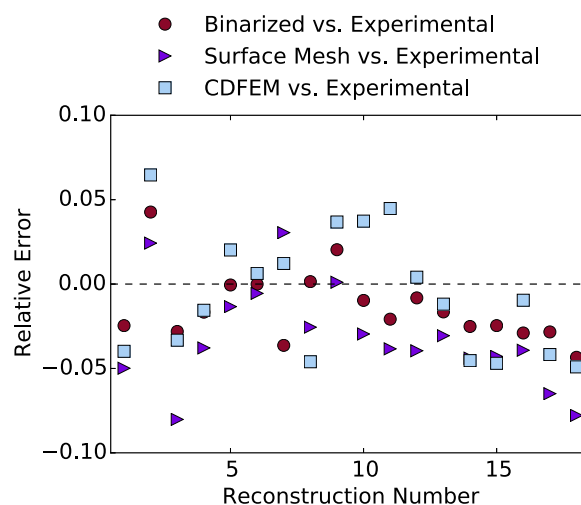


Figure A2. Relative error of the FeS_2 volume fraction, calculated with respect to experimental volume fractions.

The outcome of these verification studies demonstrate a challenging balance between MicroCT resolution, image processing, and meshing during preparation of polydisperse, irregularly-shaped geometries for simulation.

Mesh resolution.—A verification exercise was performed on one cathode reconstruction to determine how background mesh resolution affects the quality of simulation results. The mesh refinement study results indicated that the finest achievable background mesh size was $1.25\ \mu\text{m}$ for a $0.027\ \text{mm}^3$ domain, the element size and domain volume used for all simulations described in the main text. Memory limitations prevented us from achieving a finer mesh, even with 1 TB of memory on each high performance compute server. We also observed first-order convergence for the effective conductivity results, but a lack of convergence for measurements of the FeS_2 volume fraction and surface area when compared to measurements of the surface meshed microstructure. The lack of convergence for the microstructure measurements suggests that even the most resolved background mesh was insufficient to retain small features, such as gaps and particles, thus altering the microstructure represented by the conformal mesh. This affects the particle surface area, volume, volume fraction, particle contact area, and could ultimately affect the conductivity if the connectivity of the network changes significantly.

Domain volume.—We performed a study of simulation domain volume on one reconstruction using two different sets of boundary conditions to observe volume effects on the effective conductivity results. We roughly followed a method from Kanit et al.,³¹ where simulations on multiple spatially randomized domains of various sizes are used to calculate a representative volume element (RVE) for a given property, as well as the error expected for a certain domain size. For this study we applied Dirichlet and Neumann boundary conditions to obtain upper and lower effective electrical conductivity limits for our microstructure,³² respectively. We determined that greater error results from the domain size than from Dirichlet vs. Neumann boundary conditions. The domain volume study revealed that results from the $0.027\ \text{mm}^3$ domain led to nearly 9% relative error. This may be due to the large regions, or pockets, of EBLP appearing in Figure 1, which are very large compared to the full domain. To achieve 1% relative error, the domain volume must be increased to approximately $0.310\ \text{mm}^3$. The effective conductivities obtained with this simulation domain size are not truly representative of the microstructure. A 3D microstructure characterization large enough to provide a representative volume element, combined with resolution fine enough to capture the smallest features, exceeds our current imaging and computational capabilities.

Model physics.—An initial simplification made in the model physics was the electrical conductivity ratio selected for FeS_2 and EBLP. Literature values indicate that the electrical conductivity of FeS_2 at a single temperature can vary by four orders of magnitude ($0.2 \leq \sigma \leq 5623.2\ \text{1}/(\Omega\text{m})$ at 298 K).²⁷ In addition, the electrical conductivity of MgO , the binder in EBLP, can vary by eight orders of magnitude at a single temperature ($10^{-16} \leq \sigma \leq 10^{-8}\ \text{1}/(\Omega\text{m})$ at 298 K),³³ and not all solid-state electrical conductivities for EBLP components are currently available, so they were approximated as insulators ($\sigma \leq 10^{-10}\ \text{1}/(\Omega\text{m})$).³⁴ With these considerations, the $\sigma_{\text{FeS}_2}/\sigma_{\text{EBLP}}$ ratio could lie between 10^7 and $\geq 10^{19}$. We sought to simplify the problem by testing a wide range of $\sigma_{\text{FeS}_2}/\sigma_{\text{EBLP}}$ ratios ($10^1, 10^2, 10^3, \dots, 10^7$) on a simulation with a simple cubic unit cell with overlapping particles. Then, we calculated the relative error of each simulation’s effective conductivity with respect to the simulation with a 10^7 ratio, which was the most conservative ratio from the literature value approximations. We achieved relative

error <0.001 when $10^3 \leq \sigma_{\text{FeS}_2}/\sigma_{\text{EBLP}} \leq 10^6$. For this reason, we chose to simplify the problem without adding significant error by using the ratio $\sigma_{\text{FeS}_2}/\sigma_{\text{EBLP}} = 10^3$. It is critical to note that the absolute values of the conductivities used in the simulations do not matter, only the FeS_2 :EBLP conductivity ratio. The resulting effective conductivity can be scaled to any absolute value by uniformly scaling the input parameter conductivities. For these simulations we used $\sigma_{\text{FeS}_2} = 10 \text{ 1}/(\Omega\text{m})$ and $\sigma_{\text{EBLP}} = 0.01 \text{ 1}/(\Omega\text{m})$. Because we assumed steady state and a single temperature in our model setup, we treated these conductivities as constants.

In addition to each phase's electrical conductivity, in the simulations we treated the microstructure as a bicomposite material with uniform properties throughout each phase, unaffected by interparticle contact resistance or variable material properties that could be due to environmental factors (e.g., oxidation layers and contaminants). The lack of consistency between experimental and simulation results indicates that more complex model physics could be helpful, but the starting point should be improvement of the factors discussed earlier in this appendix.

References

- P. J. Masset and R. A. Guidotti, Thermal activated ("thermal") battery technology: Part IIIa: FeS_2 cathode material, *J. Power Sources*, **177**(2), 595 (2008).
- S. Ghosh and D. Dimiduk, editors. *Computational Methods for Microstructure-Property Relationships*. Springer, New York, 2011.
- A. M. Kargupikar and A. G. Vedeshwar, Electrical and optical properties of natural iron pyrite (FeS_2), *Phys. Status Solidi A*, **109**(2), 549 (1988).
- R. R. Schieck, A. Hartmann, S. Fiechter, R. Konenkamp, and H. Wetzel, Electrical properties of natural and synthetic pyrite (FeS_2) crystals, *J. Mater. Res.*, **5**, 1567 (1990).
- S. B. Lalvani, A. Weston, and J. T. Masden, Characterization of semiconducting properties of naturally occurring polycrystalline FeS_2 (pyrite), *J. Mater. Sci.*, **25**(1), 107 (1990).
- M. Au, Nanostructured thermal batteries with high power density, *J. Power Sources*, **115**, 360 (2003).
- G. L. Di Benedetto, R. R. Carpenter, D. B. Swanson, and B. D. Wightman, Enhanced nanostructuring of iron disulfide for thermal battery cathode materials, Orlando, FL, June 2014. Proc. Power Sources Conf., 46th.
- R. A. Guidotti, F. W. Reinhardt, and W. F. Hammett, Screening study of lithiated catholyte mixes for a long-life $\text{Li}(\text{Si})/\text{FeS}_2$ thermal battery, Technical Report SAND 85-1737, Sandia Natl. Lab., Albuquerque, NM, (1988).
- F. R. Brushett, M. S. Naughton, J. W. D. Ng, L. Yin, and P. J. A. Kenis, Analysis of Pt/C electrode performance in a flowing-electrolyte alkaline fuel cell, *Int. J. Hydrogen Energy*, **37**, 2559 (2012).
- D. S. Eastwood, V. Yufit, J. Gelb, A. Gu, R. S. Bradley, S. J. Harris, D. J. L. Brett, N. P. Brandon, P. J. Withers, and P. R. Shearing, Lithiation-induced dilation mapping in a lithium-ion battery electrode by 3D X-ray microscopy and digital volume correlation, *Adv. Energy Mater.*, **4**(4), (2014).
- H. Jhong, F. R. Brushett, L. Yin, D. M. Stevenson, and P. J. A. Kenis, Combining structural and electrochemical analysis of electrodes using micro-computed tomography and a microfluidic fuel cell, *J. Electrochem. Soc.*, **159**, B292 (2012).
- H. Jhong, F. R. Brushett, and P. J. A. Kenis, The effects of catalyst layer deposition methodology on electrode performance, *Adv. Energy Mater.*, **3**(5), 589 (2013).
- B. C. Larson and L. E. Levine, Submicrometre-resolution polychromatic three-dimensional X-ray microscopy, *J. Appl. Crystallogr.*, **46**(1), 153 (2013).
- S. R. Stock, Recent advances in X-ray microtomography applied to materials, *Int. Mater. Rev.*, **53**(3), 129 (2008).
- L. Zielke, T. Hutzenlaub, D. R. Wheeler, I. Manke, T. Arlt, N. Paust, R. Zengerle, and S. Thiele, A combination of X-ray tomography and carbon binder modeling: Reconstructing the three phases of LiCoO_2 Li-ion battery cathodes, *Adv. Energy Mater.*, **4**(8), (2014).
- T. Leidi, G. Scocchi, L. Grossi, S. Pusterla, C. D'Angelo, J. Thiran, and A. Ortona, Computing effective properties of random heterogeneous materials on heterogeneous parallel processors, *Comput. Phys. Commun.*, **183**(11), 2424 (2012).
- T. Fiedler, I. V. Belova, and G. E. Murch, Critical analysis of the experimental determination of the thermal resistance of metal foams, *Int. J. Heat Mass Transfer*, **55**(15–16), 4415 (2012).
- M. B. Bird, S. L. Butler, C. D. Hawkes, and T. Kotzer, Numerical modeling of fluid and electrical currents through geometries based on synchrotron X-ray tomographic images of reservoir rocks using avizo and COMSOL, *Comput. Geosci.*, **73**, 6 (2014).
- C. Sandino, D. D. McErlain, J. Schipilow, and S. K. Boyd, The poro-viscoelastic properties of trabecular bone: a micro computed tomography-based finite element study, *J. Mech. Behav. Biomed. Mater.*, **44**, 1 (2015).
- Minitab, Inc. Minitab statistical software - Minitab. Online <https://www.minitab.com/en-us/>.
- Gilson Company, Inc. ASTM Test Sieves. <http://www.globalgilson.com/astm-test-sieves>.
- Scribner Associates. Software downloads: ZPlot and ZView. Online. <http://www.scribner.com/software/scribner-associates-software-downloads/160-zplot-and-zview-for-windows-software-downloads>.
- Avizo 9 user's guide. Online, 2015. <http://www.fei.com/software/avizo-3d-user-guide.pdf>.
- D. Noble, E. Newren, and J. Lechman, A conformal decomposition finite element method for modeling stationary fluid interface problems, *Int. J. Numer. Methods Fluids*, **63**, 725 (2010).
- S. A. Roberts, V. E. Brunini, K. N. Long, and A. M. Grillet, A framework for three-dimensional mesoscale modeling of anisotropic swelling and mechanical deformation in lithium-ion electrodes, *J. Electrochem. Soc.*, **161**(11), F3052 (2014).
- Sierra Thermal/Fluid Development Team, SIERRA Multimechanics Module: Aria User Manual Version 4.40, Technical Report SAND2016-4159, Sandia Natl. Lab., Albuquerque, NM (2016).
- P. K. Abraitis, R. A. D. Patrick, and D. J. Vaughan, Variations in the compositional, textural and electrical properties of natural pyrite: A review, *Int. J. Miner. Process.*, **74**(1–4), 41 (2004).
- B. G. Streetman, *Solid State Electronic Devices*, Prentice Hall, Englewood Cliffs, NJ, 3rd edition, 1990.
- A. P. Chandra and A. R. Gerson, The mechanisms of pyrite oxidation and leaching: A fundamental perspective, *Surf. Sci. Rep.*, **65**, 293 (2010). (accessed Aug 26, 2015).
- N. Gunda, C. Hae-Won, A. Berson, B. Kenney, K. Karan, J. Pharoah, and S. Mitra, Focused ion beam-scanning electron microscopy on solid-oxide fuel-cell electrode: Image analysis and computing effective transport properties, *J. Power Sources*, **196**, 3592 (2011).
- T. Kanit, S. Forest, I. Galliet, V. Mounoury, and D. Jeulin, Determination of the size of the representative volume element for random composites: Statistical and numerical approach, *Int. J. Solids Struct.*, **40**, 3647 (2003).
- M. Ostojca-Starzewski and J. Schulte, Bounding of effective thermal conductivities of multiscale materials by essential and natural boundary conditions, *Phys. Rev. B*, **54**, 278 (1996).
- D. Sangeta and J. R. LaGraff, *Inorganic Materials Chemistry Desk Reference*. CRC Press, Boca Raton, FL, 2nd edition, 2005.
- W. D. Callister, *Materials Science and Engineering: An Introduction*. John Wiley & Sons, Inc., New York, 4th edition, 1997.